Investigation of Regional and Seasonal Variations in Marine Boundary Layer Cloud Properties from MODIS Observations

MICHAEL P. JENSEN AND ANDREW M. VOGELMANN

Brookhaven National Laboratory, Upton, New York

WILLIAM D. COLLINS

Lawrence Berkeley National Laboratory, Berkeley, California

GUANG J. ZHANG

Scripps Institution of Oceanography, La Jolla, California

EDWARD P. LUKE

Brookhaven National Laboratory, Upton, New York

(Manuscript received 28 March 2007, in final form 8 February 2008)

ABSTRACT

To aid in understanding the role that marine boundary layer (MBL) clouds play in climate and assist in improving their representations in general circulation models (GCMs), their long-term microphysical and macroscale characteristics are quantified using observations from the Moderate Resolution Imaging Spectroradiometer (MODIS) instrument aboard the National Aeronautics and Space Administration's (NASA's) *Terra* satellite. Six years of MODIS pixel-level cloud products are used from oceanic study regions off the west coasts of California, Peru, the Canary Islands, Angola, and Australia where these cloud types are common. Characterizations are given for their organization (macroscale structure), the associated microphysical properties, and the seasonal dependencies of their variations for scales consistent with the size of a GCM grid box (300 km $\times$ 300 km). MBL mesoscale structure is quantified using effective cloud diameter C_D, which is introduced here as a simplified measure of bulk cloud organization; it is straightforward to compute and provides descriptive information beyond that offered by cloud fraction. The interrelationships of these characteristics are explored while considering the influences of the MBL state, such as the occurrence of drizzle.

Several commonalities emerge for the five study regions. MBL clouds contain the best natural examples of plane-parallel clouds, but overcast clouds occur in only about 25% of the scenes, which emphasizes the importance of representing broken MBL cloud fields in climate models (that are subgrid scale). During the peak months of cloud occurrence, mesoscale organization (larger C_D) increases such that the fractions of scenes characterized as "overcast" and "clumped" increase at the expense of the "scattered" scenes. Cloud liquid water path and visible optical depth usually trend strongly with C_D, with the largest values occurring for scenes that are drizzling. However, considerable interregional differences exist in these trends, suggesting that different regression functionalities exist for each region. For peak versus off-peak months, the fraction of drizzling scenes (as a function of C_D) are similar for California and Angola, which suggests that a single probability distribution function might be used for their drizzle occurrence in climate models. The patterns are strikingly opposite for Peru and Australia; thus, the contrasts among regions may offer a test bed for model simulations of MBL drizzle occurrence.

Corresponding author address: Dr. Michael P. Jensen, Atmospheric Sciences Division, Brookhaven National Laboratory, Bldg. 490D, Upton, NY 11973-5000.
E-mail: mjensen@bnl.gov

DOI: 10.1175/2008JCLI1974.1

1. Introduction

Marine boundary layer (MBL) clouds represent a climatologically significant influence on the global energy and water cycle (Randall et al. 1984). Because they possess an albedo that is much larger than the underlying ocean surface, these clouds cause a significant decrease in the amount of solar radiation absorbed in the ocean's mixed layer, with minimal compensation in thermal radiation emitted to space. In fact, observations of the top-of-atmosphere radiation balance measured by the Earth Radiation Budget Experiment (ERBE) satellite and the cloud fields observed by the International Satellite Cloud Climatology Project (ISCCP) show that low clouds provide the largest net radiative cloud forcing of any cloud type (Hartmann et al. 1992). Despite their importance, the albedo of subtropical MBL clouds is poorly simulated by climate models (Zhang et al. 2005; Bender et al. 2006). It has even been shown that their simulation and response to changing environmental conditions is the main source of uncertainty in tropical cloud feedbacks simulated by climate models (Bony and Dufresne 2005). These radiative impacts are influenced by both macro- and microphysical properties of the clouds that are not fully understood, and their accurate representation in climate models is essential for obtaining realistic simulations.

The nature of this problem is shown in Fig. 1, which illustrates the complex structure that often exists within MBL cloud regions. General circulation models (GCMs) that are used for long-term climate simulations typically have a horizontal grid resolution of approximately 300 km; so dramatic variations in MBL cloud structure are possible even within one model grid cell. Such variations clearly have important impacts on the albedo of the system, and understanding them will require a description of how the cloud field is organized (on the macroscale), the associated microphysical properties (e.g., liquid-water path and drop size), as well as their dependence on the atmospheric physical, dynamic, and thermodynamic properties.

For some time, satellite-borne instrumentation has provided the means for observing the intricate structure of MBL cloud fields (e.g., Agee 1984). The description of these fields continues to improve with the deployment of more advanced sensors (e.g., Garay et al. 2004), as well as through the considerable advances in retrieving cloud properties from the measured radiances (e.g., liquid water path and cloud drop size). However, despite these advances, the cloud properties normally available to the broader climate modeling community involve bulk properties such as cloud fraction, which is certainly not sufficient to quantify this structure. A notable exception is the recent work by Wood and Hartmann (2006), who developed a neural net to use pixel-level satellite data to classify the MBL mesoscale cellular convection (MCC) within scenes (e.g., no MCC, closed MCC, open MCC, cellular but disorganized). Their study was performed for 2 months of data for regions off the coasts of California and Peru.

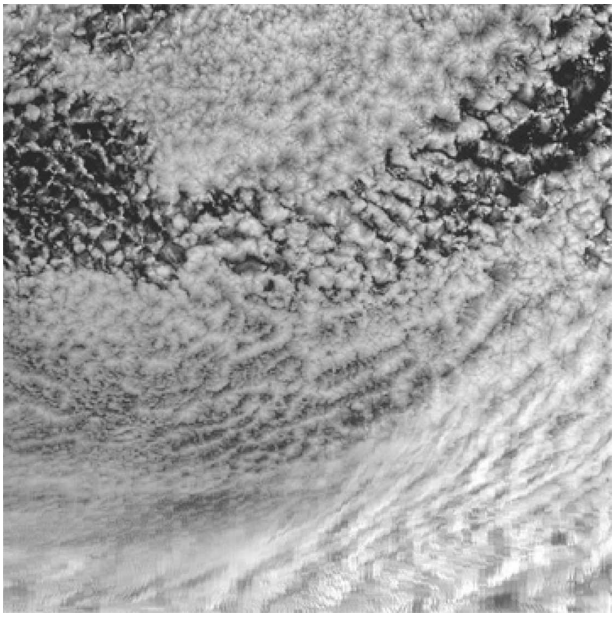

FIG. 1. Marine boundary layer cloud scene. This *Terra* MODIS scene illustrates the complex structure that often exists within MBL cloud regions. The region shown is about 750 km on each side and is from off the coast of California on 2 Jan 2005. The image uses reflected radiances for MODIS band 3.

As such additional cloud structure information becomes available, its utility to the modeling community depends on it being represented (packaged) in variables that can be related to those used in the climate models. The cloud property variations seen in Fig. 1 occur at a scale that is much finer than the model resolution; however, the figure also shows that similar fine-scale variations occur across regions that are much larger than the individual variations. These features suggest that the governing processes may interact with the mesoscale through mechanisms that could be represented even at the relatively low resolution of most current climate models. For example, Cusack et al. (1999) showed, using a high-resolution forecasting model, that the subgrid-scale variance of cloud and atmospheric properties with a GCM grid box can be parameterized from larger-scale variations that are resolved by the GCM.

The physical processes that are responsible for structures seen in the MBL cloud fields are not fully under-

stood, but recent research has indicated that the occurrence of drizzle may play a key role in forming and sustaining the observed structures. Observational studies have investigated pockets of open cells (POCs) that are embedded in otherwise uniform stratocumulus, and resemble broader regions of open mesoscale cellular convection typically found farther offshore (Stevens et al. 2005). POCs and open mesoscale cellular convection are long lived and contain pronounced amounts of drizzle, which is in contrast to the substantially smaller amount of drizzle found in the surrounding unbroken, stratiform MBL clouds (Comstock et al. 2007). Large-eddy simulation (LES)-based studies support that, when drizzle processes are included, mesoscale organization emerges in the form of cloud bands as the well-mixed MBL (with stratiform cloud) transitions into a convective boundary layer regime (Mechem and Kogan 2003). In addition to the greater amounts of drizzle and mesoscale variability, the POCs also differ microphysically from the stratiform MBL cloud regions by having a smaller amount of liquid water and larger effective radii (Wood and Hartmann 2006). Evidence suggests that the differences in precipitation amounts between the POCs and stratiform regions may be caused by different amounts of cloud condensation nuclei available from aerosols (Sharon et al. 2006; Petters et al. 2006; Rosenfeld et al. 2006), where the effects may depend on the combined influences of aerosols, thermodynamics, and the diurnal cycle (Matsui et al. 2006).

In this paper, to aid in understanding the role MBL clouds play in climate and assist in improving their representations in climate models, we use satellite data to characterize the organization of MBL cloud systems across the globe (macroscale structure), their associated microphysical properties (e.g., liquid water path and particle size), and the seasonal dependence of their variations. The interrelationships of these characteristics are explored while considering the influences of the MBL state, including the occurrence of drizzle. While many prior studies have investigated MBL cloud properties for either a specific region or a limited period, additional insights can be obtained by examining global and seasonal (long term) differences, as has been done by studies that used either ship-based observations (e.g., Klein and Hartmann 1993; Norris and Leovy 1994) or satellite data (Rozendaal and Rossow 2003). Our analyses use six full years of satellite data from the Moderate Resolution Imaging Spectroradiometer (MODIS) aboard the National Aeronautics and Space Administration's (NASA's) *Terra* satellite to examine the seasonal interregional differences in MBL cloud properties in five oceanic regions where these cloud types are typical. Similar to other work (e.g., Xu et al. 2005; Zhou et al. 2006), we construct probability distribution functions (PDFs) of many of the properties as a means to quantify the property variation across the region. As will be seen, we use extensive amounts of pixel-level satellite data to enable screening and analyses that would not be possible with coarser (gridded) datasets, such as quantifying the cloud–to–cloud scale (macroscale) structure within each MBL scene. The intended use of these relationships is to aid in improving GCM representations of MBL clouds through simulation evaluation and parameterization development of these MBL cloud characteristics.

The study is presented as follows: Section 2 describes the pixel-scale MODIS cloud property retrievals used, including considerations and minor modifications applied to their values. Section 3 describes the methodology, which includes the location of the MBL study regions used, and the procedures used to select and screen for MBL scenes of the area of a GCM grid box (300 km $\times$ 300 km). Special attention is given to steps taken to minimize the potential uncertainty in the cloud microphysical retrievals that can be caused by partially filled cloud pixels or 3D effects. This section also describes the calculation of the effective cloud diameter, which we use to quantify the bulk cloud–to–cloud scale structure within each scene. The measure it provides of the cloud macroscale structure is coarse; however, it is simple to compute and provides cloud structure information beyond that available from cloud fraction, yet can be approximated by grid-scale variables computed in GCMs. Section 3 contains the results of the analysis that uses six full years of satellite data for multiple MBL cloud regions, and includes differences in the regional and seasonal variations of cloud diameter. We explain how drizzle occurrence is determined from the data, and show how its regional and seasonal variations are related to those in cloud diameter and the cloud microphysical properties (e.g., liquid water path, drop size, and optical depth). The objective of this study is to determine the seasonal and regional variations that exist in cloud macroscale structure (cloud diameter), drizzle frequency, and their associated microphysical properties, such that they may be used in GCM climate model validation and parameterization development. It is beyond the scope of this study to determine how these interrelationships impact the radiative budget or are affected by factors such as the meteorological state and aerosol properties, which will be the subject of later research.

2. *Terra* MODIS data

The data used are from the MODIS instrument deployed on NASA's *Terra* satellite that was launched on

18 December 1999. *Terra* is a sun-synchronous, polar-orbiting satellite that has an equatorial overpass at approximately the same local time (LT) once daily in the ascending (2230 LT) and descending (1030 LT) nodes. The orbit precesses to provide a view of the entire earth's surface every 1–2 days. We only use data from the 1030 LT overpass because many of the MODIS retrievals we use require solar illumination. The *Terra* MODIS data collection began in February 2000. Each scan consists of a 2330-km swath of upwelling radiance measurements in 36 spectral bands from 0.4 to 14.4 μm that have horizontal resolutions ranging from 250 to 1000 m. The MODIS Atmosphere Team uses combinations of these spectral observations to determine a cloud mask and retrieve cloud physical and radiative properties (Platnick et al. 2003; King et al. 2003). We use version 4 of the MODIS instantaneous pixel-level cloud product retrievals (MOD06_L2). With the analysis methodology we employed (described next section), negligible differences were found in most of our MBL cloud statistics when results using version 4 MODIS cloud products were compared with those using version 5. The single exception is for effective cloud diameter, which is easily understood and discussed later in the relevant section.

The primary MODIS products used here include the cloud mask, the midvisible cloud optical thickness (τ_{vis}, at 0.66 μm), liquid water path (LWP), and hydrometeor effective radius (R_{eff}). These data are provided at a nadir resolution of 1 km. The MODIS team derives τ_{vis} and R_{eff} using radiances from three water-absorbing bands (1.6, 2.1, 3.7 μm) and one of three nonabsorbing bands (0.65, 0.86, 1.2 μm), based on a library of results for plane-parallel homogeneous liquid and ice clouds (Platnick et al. 2003). The LWP is derived from these quantities using the relation $\text{LWP} = 2/3\rho\tau_{\text{vis}}R_{\text{eff}}$ (King et al. 1998), where ρ is the density of water. (The MODIS version 4 processing inadvertently used 3/4 instead of 2/3, which we corrected as per the "Known Problems" documentation available online at http://modis-atmos.gsfc.nasa.gov/MOD06_L2/qa.html). For the purposes of cloud screening, we use the MODIS cloud-top pressures (CTPs) that, for clouds below 700 hPa, are determined by comparing the 11-μm infrared window brightness temperature with a temperature profile from the National Centers for Environmental Prediction (NCEP) analyses (Menzel et al. 2002).

We modified the cloud mask to classify pixels with $\text{LWP} < 3$ g m^{-2} as invalid data, because visual inspection suggested that those retrievals were suspect. The MODIS cloud mask includes classifications of "certainly cloudy" and "likely cloudy," and the MODIS products are only retrieved for the certainly cloudy pixels. We use both classifications to determine our cloud boundaries, but accept the scene only if the certainly cloudy pixels are a significant fraction of the (total) cloudy pixels. This ensures that the cloud mask used for the cloud fraction (and, as discussed later, cloud diameter) is relatively insensitive to the partitioning between the "certain" and "likely" classifications and, because retrievals are only available for certainly cloudy pixels; this also ensures that the retrievals exist for the vast majority of the cloudy pixels used. The threshold requires that the ratio (certain to total cloudy pixels) is in the top 90th percentile certainty for all observations. The threshold, which varies slightly with cloud fraction, is always greater than 0.85 and is usually greater than 0.95, which means that the microphysical properties have been retrieved for most of the cloudy pixels.

Deriving LWP from the cloud optical depth and R_{eff} depends on assumptions about the cloud vertical structure. The equation above makes the common assumption that the liquid water content (LWC) and R_{eff} are constant with height. However, R_{eff} is representative only of the cloud top, and a proper retrieval of LWP would require the in-cloud profile of R_{eff} (e.g., Chang and Li 2003). Wood and Hartmann (2006) note that observations of MBL clouds indicate that LWC often increases linearly with height from cloud base while cloud droplet concentrations remain approximately constant. They conclude that a more appropriate equation for boundary layer clouds is $\text{LWP} = 5/9\rho\tau_{\text{vis}}R_{\text{eff}}$, which results in LWPs that are 0.83 times those that assume constant LWC and R_{eff} with height. This approach is valid for MBL clouds, although observations indicate that it would not be valid for continental boundary layer clouds (Miles et al. 2000). Because this paper deals only with marine boundary layer clouds, we adopt and apply the 0.83 factor to the (corrected) MODIS LWP.

3. Methods and analysis

a. Marine boundary layer study regions

We focus our attention on five major subtropical MBL cloud study regions. The general regions are the same as those identified in Loeb and Coakley (1998), but whose areas were expanded based on the ship-based observer climatologies shown in Klein and Hartmann (1993) and Norris and Leovy (1994). The additional area allows for capturing the MBL cloud decks within our MODIS study regions, because their locations during the MODIS observation period might fluctuate relative to their climatology. The five study regions and their latitudes and longitudes are given in Table 1 and are displayed in Fig. 2. Cloud data over any

TABLE 1. MBL study regions. The latitude and longitude boundaries are given for each study region. A MBL scene is defined as a 300 km × 300 km grid box that satisfies the selection criteria given in the text. The three peak months refer to the three contiguous months that contain the maximum number of MBL scenes per region. The locations of the regions are plotted in Fig. 2. A total of 38 550 independent MBL cloud scenes are identified in our 6-yr dataset spanning March 2000–February 2006.

Region name	Latitude/longitude bounds		Total number of MBL scenes	Peak 3 months
Angola	−25° to 0°N	−20° to 15°W	13 136	September–November
Australia	−40° to −15°N	85° to 115°W	4210	December–February
California	20° to 40°N	−140° to −115°W	4835	July–September
Canary Islands	5° to 30°N	−45° to −10°W	4727	May–July
Peru	−35° to 5°N	−100° to −70°W	11 642	July–September

land surface areas that might intersect the regions are removed from the analysis.

Our objective is to analyze the MBL cloud properties for these five regions throughout multiple seasonal cycles of MODIS observations to enable analyzing cloud occurrence and variations in their microphysical and macrophysical properties. To do so, we acquired 6 yr of the pixel-level *Terra* MODIS cloud products (MOD06_L2) for our regions from March 2000 to February 2006 from the Goddard Distributed Active Archive Center (DAAC). The data are obtained from the DAAC in the form of granules (the approximate size of a granule is 2030 km × 1354 km), and the parts of the granules that were within one of our study regions (Fig. 2) were subset and stored for later analysis. Overall, this process involved acquiring about 4.7 Tbytes of MOD06_L2 data from the DAAC.

b. Scene selection

Our goal is to investigate the mean properties of MBL clouds and their associated variability on the scale of a GCM grid box. The size of the grid box used here is 300 km on each side, which is the size typically used by GCMs for long-term climate simulations. One of the reasons for working with the volume-intensive pixel-level MODIS products, rather than the less voluminous gridded data (e.g., level-3 data), is to enable careful selection and quality control of our MBL scenes. Each data file acquired from the DAAC potentially contains multiple candidate MBL scenes (i.e., one scene per grid box), which are located and evaluated (quality controlled) using an automated set of procedures. A candidate scene is located within a granule by moving a 300 km × 300 km window across the region in a stepwise search pattern. If a candidate scene satisfies the criteria for a MBL scene, its pixels are removed from the search array to prevent being reused in later scenes, thereby ensuring that each scene is independent.

A candidate scene is first screened using MODIS quality control flags and solar geometry requirements. Any portion of the file that contains sun glint is excluded, because it may render cloud retrievals in that

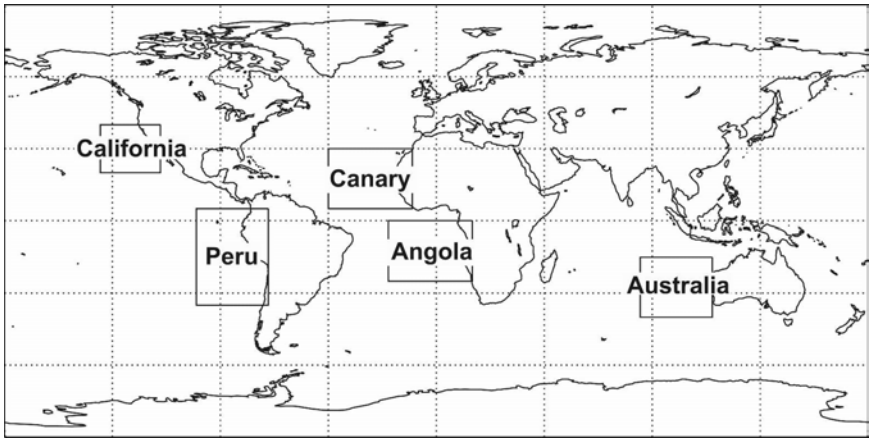

FIG. 2. Map of MBL cloud study regions. Each box indicates the location of a major MBL cloud region, based on the surface-based climatologies in Klein and Hartmann (1993) and Norris and Leovy (1994). The latitude–longitude bounds for each region are given in Table 1. Six years of data are obtained for each study region, spanning March 2000–February 2006. Cloud data over any land areas within the study regions are removed from the analyses.

region suspect. In some cases, this can exclude half of the data within the file. This has a benefit of also removing data from the forward-scattering direction that can have biases in cloud optical depth retrievals resulting from variations in cloud-top topography (Loeb and Coakley 1998). To avoid retrieval problems associated with low sun angles (Loeb and Davies, 1996), the solar zenith angle and satellite viewing angles are required to be less than 60°. A minimum cloud fraction of 20% is required, and 90% of a scene's cloud pixels must be valid (i.e., not invalid by the MODIS quality control flags).

Scenes containing significant amounts of other cloud types are rejected. For example, regions containing cirrus cloud fractions greater than 10% are rejected, because it is uncertain that thin cirrus overlying MBL clouds can be detected reliably. To determine whether MBL clouds are the dominant cloud type within a scene, each scene is tested for the presence of low cloud decks with uniform cloud-top heights. This is determined by requiring that the median CTP of the pixels is greater than 650 hPa, and that 50% of the CTPs are within ±10 hPa of the median. This removes scenes that may contain frontal cloud systems or a significant number of penetrating convective clouds. We note that a CTP of 650 hPa is higher in the atmosphere than expected for MBL clouds; however, this is only used as an upper limit for candidacy and those that are selected are much lower in the atmosphere, which is more consistent with typical MBL cloud heights. When a scene is accepted, any remaining pixels that have pressures less than 650 hPa are flagged as invalid for our analysis. This way, if we have a scene dominated by MBL clouds, but including one penetrating convective cell (<10% of the cloud pixels), the statistics for the MBL portion can still be used. We note that the CTP reported as part of the MODIS cloud product is subject to uncertainties likely resulting from problems the algorithm has with matching the observed brightness temperature to a unique atmospheric level in the presence of a strong subsidence inversion (Naud et al. 2005; R. E. Holz 2007, personal communication); however, the values obtained are still useful for determining when low cloud is present and gross features, such as frontal slopes and penetrating convection, can be eliminated because of their much lower CTPs. A final criterion requires that the cloud effective diameter be relatively constant across the scene, and is described in section 3e.

c. *Seasonal and diurnal aspects of MBL scene occurrence*

Based on these selection criteria, a total of 38 550 independent MBL cloud scenes are identified within our 6-yr dataset. The total number of scenes per region is given in Table 1, and the annual cycles of the number of scenes per region are plotted in Fig. 3a. A clear seasonal cycle is found per region, which may be considered as a rough proxy for MBL cloud occurrence. The number of monthly scenes per region can differ from each other by a factor of 3 or more (Fig. 3a). This can be explained by the different sizes in the study regions (see Table 1), and by the variable fraction of a region's "true" MBL frequency accepted by our analysis after rejecting scenes that are contaminated by high clouds or other quality control issues. The fraction of true MBL scenes rejected by such issues will vary between regions and even within a region over its seasonal cycle. Our satellite sampling will be biased toward cases dominated by high pressure systems, because our method rejects scenes containing a significant number

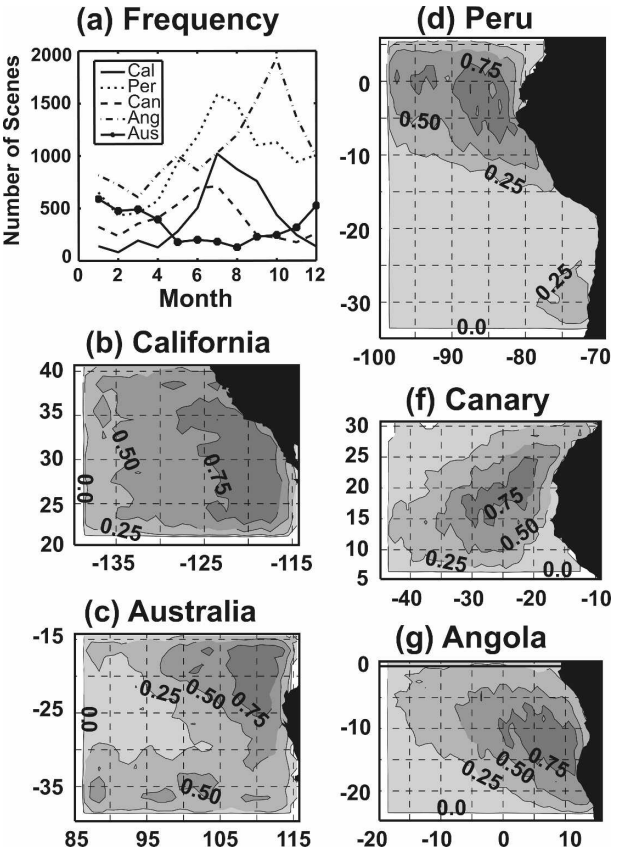

FIG. 3. Occurrence frequencies of MBL cloud scenes. (a) Monthly frequencies per region. The numbers of MBL cloud scenes identified per month are combined from all years. (b)–(f) Regional variations in MBL cloud scene occurrence. For each region, the number of MBL scenes for all months are combined and gridded. Results are displayed as a fraction of the respective region's maximum grid value (i.e., the maximum value in each 2D plot is one). Occurrence frequency per region is binned on a 1° grid.

of high-level clouds (10% of cloudy pixels). During peak months, large-scale subsidence generally exists within our regions, which diminishes the chance of high-level clouds; however, this is not the same case during off-peak months, which increases the chances of scene rejection. Because of seasonal differences in high cloud occurrence, the seasonal patterns shown in Fig. 3a may be thought of as being representative of the MBL cloud frequency, but they cannot be translated directly into absolute seasonal cycles in MBL cloud occurrence.

For example, Klein and Hartmann (1993) used 30 yr of ship-based observer reports (Woodruff et al. 1987) to define climatologies for similar regions. They find a stratus maximum in the Peru region around −20°S, where we find a local minimum between the northern and southern maxima. However, an inspection of ISCCP cloud data reveals that midlevel clouds tend to occur in this region with a maximum over the southern portion of our defined region (from about −15° to −30°S). For cases where MBL clouds are mixed with midlevel clouds, we would reject the scene to avoid contaminating our MBL cloud properties with those from the midlevel clouds. Differences from Klein and Hartmann may also arise because we do not limit our definition of MBL clouds to large cloud fraction scenes. We allow MBL scenes to be identified with cloud fractions as low as 20%, which includes the transition region, and possibly the trade cumulus regions, that might be classified differently in other cloud climatology studies. We feel these cloud systems should be included because they are present within a continuum of dynamical conditions within the MBL.

Nevertheless, despite these differences, the seasonal cycle that is found generally agrees well with that observed by Klein and Hartmann (1993). The months of peak MBL cloud frequency are easily identified and are listed in Table 1, and only minor amounts of interannual variability exist within our seasonal cycles (not shown). We find similar peak months to those in Klein and Hartmann (1993) for three of the five regions (Canary Islands, Angola, and Australia); however, the peaks are slightly shifted for California (theirs are June–August and ours are July–September) and Peru (theirs are September–November and ours are July–September). These differences could be caused by the following several obvious differences in the observation methods: the locations of the study regions are slightly different (their regions are subsets of our larger regions); unlike the ship-based observations, our satellite algorithm rejects scenes that are contaminated by high-level clouds or sun glint; there are possible differences caused by the diurnal sampling between the ship-based observations and the *Terra* satellite midmorning observation time; and our 6-yr study period is not equivalent to the 30-yr period they used for their climatology. Also included in Fig. 3 are the geographical distributions of the MBL cloud occurrence within each region, which show that the maxima are generally captured well within our study regions. These distributions have combined all years into a single image, but the general locations of the maxima do not shift significantly during the seasonal cycle (not shown) although, of course, their absolute magnitudes are modulated by the seasonal cycle in the total number of scenes given in Fig. 3a.

Klein and Hartmann (1993) concluded from their analysis that the annual cycle of MBL cloud occurrence is closely tied to the annual cycle of static stability in the lower atmosphere. MBL clouds are also influenced by the diurnal cycle of factors, such as boundary layer mixing and cloud-top entrainment, which are driven by the differential solar heating and infrared cooling at cloud top. Generally speaking (e.g., summarized in Comstock et al. 2005), at nighttime, infrared cooling causes air parcels to sink, and they tend to mix (couple) the MBL, as well as entrain drier air aloft at cloud top. As daytime progresses, solar radiation heats the cloud top and reduces the effects of infrared cooling. This reduces the amount of mixing within the MBL and, in particular, below cloud base. This solar heating, assisted possibly by drizzle in the early morning, can ultimately lead to decoupling of the MBL, whereby the mixing no longer extends through the depth of the MBL (i.e., across the cloud and surface air layers). At nighttime, the infrared cooling reenergizes the MBL mixing (coupling). While this is a broad conceptual view of the diurnal cycle, it is useful to bear in mind that the results presented using data from the *Terra* satellite will tend to capture the midmorning state of this diurnal cycle, which is generally a transition period between the coupled and decoupled states.

d. Acquiring scene statistics and uncertainties

For each scene that passes this rigorous screening, we compute its cloud fraction and the mean of the cloud pixels for τ_{vis}, LWP, and R_{eff}. In addition to the items discussed earlier, these cloud property retrievals can be effected by uncertainties caused by some other considerations that are addressed here. For example, retrievals of cloud properties from satellite data often assume that the cloud within each pixel is overcast, as is assumed for the MODIS retrievals. However, some pixels might only be partially cloud covered and, if so, they would masquerade to a retrieval algorithm as a thinner cloud (e.g., Oreopoulos and Davies 1998). This would

lead to overestimations in cloud amounts and R_{eff}, while underestimating visible optical depths and cloud LWP (Coakley et al. 2005). To minimize the potential impact of this uncertainty, we use a binary cloud mask to locate pixels that reside at the edge of the cloud, and remove them from our calculations of the mean. From the edge, we remove only one pixel deep into the cloud. We acknowledge that all of these pixels might not be partially cloud filled and that we might be excluding legitimate cloud variability that exists at cloud edge. However, at least part of this variability will be captured by the neighboring cloud pixels that are not removed, while erroneous retrievals of potentially partially filled pixels would introduce biases with little to no compensation. For the calculation of cloud fraction, we have no choice but to use the MODIS cloud mask as is (i.e., include potential partially filled pixels) because its exclusion would only guarantee an underestimation of the cloud fraction.

The MODIS cloud retrieval algorithm also makes the common assumption that the radiance field emerging from the cloud can be accurately interpreted using plane-parallel radiative transfer theory. This assumes that 3D radiative transfer effects are negligible, whether they are pixel-to-pixel exchanges of photons or shadowing of pixels by uneven cloud-top topography (e.g., Marshak et al. 2006). The presence of such 3D effects can result in retrieval errors in cloud optical depth (Loeb and Davies 1996; Loeb and Coakley 1998; Várnai and Marshak 2002a,b) as well as R_{eff} (Bréon and Doutriaux-Boucher 2005; Cornet et al. 2005; Marshak et al. 2006). Correcting these potential 3D effects for all of our study regions is beyond the scope of this study. However, we note that the following considerations will reduce the systematic effect of retrieval artifacts related to 3D cloud geometry: 1) exclude the pixels at the edge of the cloud, because 3D effects are arguably the largest at a cloud edge; 2) seek the central tendency (average) for a scene that is 300 km on each side so that a certain amount of cancellation of 3D effects of opposite sign can be expected in the averaging; 3) note that the tops of many MBL clouds follow the top of the smoothly varying boundary layer inversion (e.g., except for the case of decoupling), and 4) use only scenes that have a cloud fraction of 20% or more, which would tend to avoid cumulus fields that are particularly problematic (e.g., Marshak et al. 2006). Our approach seems to be supported by the recent work of Vant-Hull et al. (2007), who show that 3D effects on MODIS retrievals of effective radius are reduced by the combined contributions of removing one pixel from cloud edges and averaging the results across a large area (e.g., as for our 300-km grid boxes). Further, at least one piece of circumstantial evidence suggests that the effects of such 3D effects are minimized after augmenting the algorithm and quality control practices used in the MODIS products with our analysis procedure. Marshak et al. (2006) show that, because retrievals using plane-parallel theory cannot treat the shadowing of neighboring pixels caused by cloud-top height variations, such cases will retrieve optical depths that are biased low and R_{eff} that are biased high. However, as will be seen later herein, we find the opposite pattern (i.e., larger optical depths for scenes correlate with larger R_{eff}), which is also in general agreement with related marine boundary layer observations.

e. Effective cloud diameter

The eventual goal of this work is to aid GCM cloud parameterization, and to assist in this endeavor we desire a property that goes beyond determining the fractional cloud coverage of the scene and quantifies the bulk cloud-to-cloud-scale structure within each scene. Information on how the cloud elements are organized within the scene may offer useful descriptive information beyond cloud fraction, because their horizontal distribution might result from (or impact) cloud-top entrainment and/or the state of the MBL coupling/decoupling. To quantify how the clouds within a scene are organized or clustered, we compute its effective cloud diameter C_D. It is proportional to the average diameter of the clouds within the scene and is defined as

$$C_D = \frac{4\sum_{i}^{N} A_i}{\sum_{i}^{N} P_i}, \tag{1}$$

where A_i and P_i are, respectively, the area and perimeter of the N individual clouds within the scene. (A cloud is a contiguous set of cloud-filled pixels that is surrounded by a ring of cloud-free pixels.) The factor of 4 converts the ratio to a cloud diameter, such that for a scene containing perfectly circular clouds with diameter D, C_D would equal D. Figure 4 shows an idealized example of C_D and its advantage relative to using the cloud fraction. Each scene is composed of circular clouds, whose radii are the same, that change among scenes. Even though the cloud fraction is identical for all scenes, C_D varies by a factor of 2 from 0.75 arbitrary length units (lu) to 1.5 lu. Thus, C_D provides information additional to the cloud fraction about how clouds are organized within a scene.

The calculation of C_D is generally insensitive to the

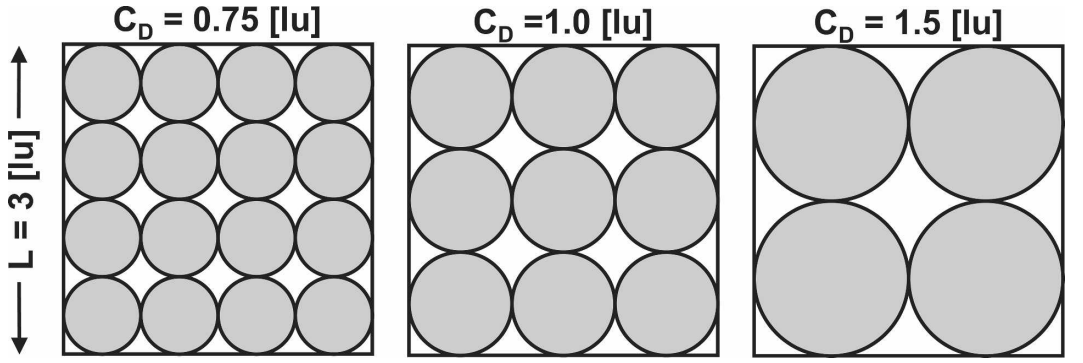

FIG. 4. Idealized illustration of effective cloud diameter. For each scene composed of circular clouds, the cloud fraction is constant at 0.785, but C_D assumes a different value for each scene: 0.75, 1.0, and 1.5 lu. This shows how C_D provides information additional to cloud fraction about how clouds are organized within a scene.

size of the scene (or grid). It is completely insensitive to the size of the scene when the individual clouds are small enough to remain within (and not cross) the scene perimeter; however, the maximum value for C_D is limited by the size of the scene. This limit applies when a single large cloud fills the scene completely. In our study, with square scenes 300 km on each side, the values for C_D range from near zero (very scattered clouds) to a maximum of 300 km (a single, solid cloud deck, or "sheet," without any holes). Examples of different cloud scenes from MODIS observations and how they are quantified via C_D are given in Fig. 5 for MBL clouds off the coast of California. We emphasize that the calculation of C_D depends only on the scene's binary cloud mask, and not on the LWP variations among the cloudy pixels. This simplicity lends itself to the speed and stability needed for our multiyear, automated analysis and, as will be seen, C_D correlates well with the properties currently available from GCMs, such as cloud fraction and LWP.

The calculation of C_D is robust in that it can be easily calculated for any scene with minimal numerical chatter. Except for the limit when a single cloud approaches filling the entire scene, tests of C_D find that it is fairly independent of the scene size used. We tested the stability of C_D by starting with 300 km $\times$ 300 km scenes, and we "zoomed" in via multiple size steps, recomputing C_D at each step. Regardless of the initial C_D value, it remained roughly constant until the grid approached 100 km. The only exception was if the scene happened to be centered on the edge of a cloud system where, for example, half of the scene is overcast and the other half is clear. However, because the cloud character is not consistent across the scene, it also would not be desirable (representative) input for our analysis. So, as a final scene selection criterion (in addition to those in section 3b), we use this zoom procedure to remove scenes that contain cloud edges, and require that the C_D value remain constant to within 50% when the scene is zoomed in by 50% (i.e., 300–150 km). We tested the sensitivity of C_D calculations to using MODIS version 4 versus version 5 cloud products. The C_D frequency distributions shift slightly toward larger values when version 5 data are used, with the peak increasing by about 20 km. Such a difference would not change the conclusions discussed in this work, and would not be obvious in the graphs because C_D is plotted on a logarithmic scale.

f. *Relation of cloud diameter to cloud fraction and cloud structure*

For the use of our analysis for GCM parameterization and validation efforts, C_D does not need to be computed within a GCM. Rather, it is primarily used here as a means to separate the different classes of cloud fields. However, we do find a general relationship between MBL scene cloud fraction (computed in GCMs) and C_D, which may be useful for translating between the two. Figure 6a shows how C_D increases with cloud fraction, where the points represent binned medians of all of the MBL cloud scenes in our database. In the limit of large cloud fractions, C_D has a greater range of values and, therefore, provides a more sensitive measure of bulk cloud structure than cloud fraction. A sigmoidal fit to the median points is shown for reference, and the coefficients of the fit are provided. The fit is only applicable within the bounds of the data used for the fit, $5 \leq C_D \leq 300$ km, where the lower limit (cloud fraction of 0.35) arises from the limit we set for screening and identifying MBL scenes from other types of clouds. The fit is better than ± 0.015 in cloud fraction, and the average of the absolute deviation between all median points and the fit is within 0.0017. The relation-

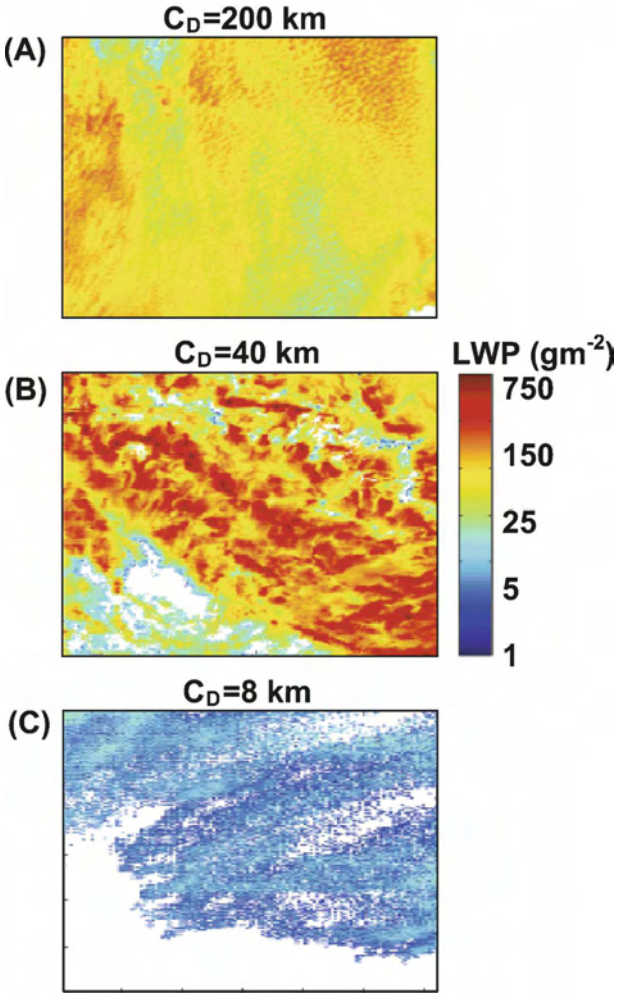

FIG. 5. Marine stratus cloud structure and effective cloud diameter. The three MODIS scenes illustrate the appearance of the cloud LWP as C_D increases sequentially by a factor of 5 between each scene. Plotted are $\log_{10}$(LWP), where white is clear sky. For each scene, the effective cloud diameter, fractional cloud cover, mean cloud LWP, and standard deviation of the LWP are (a) C_D = 200 km, f = 99%, L = 81 g m^{-2}, σ = 35 g m^{-2}; (b) C_D = 40 km, f = 83%, L = 189 g m^{-2}, σ = 132 g m^{-2}; and (c) C_D = 8 km, f = 51%, L = 9.7 g m^{-2}, σ = 4.3 g m^{-2}.

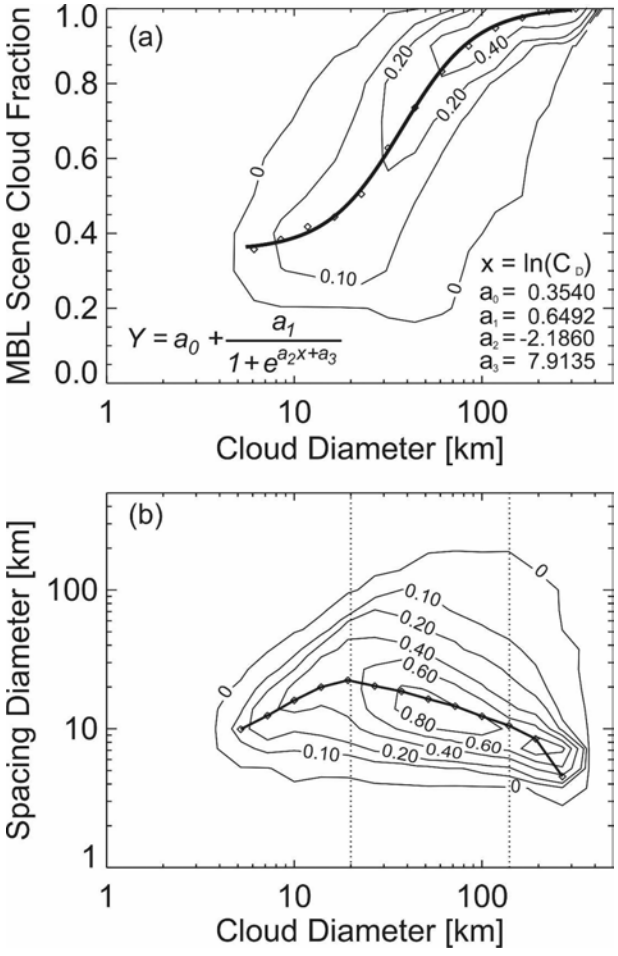

FIG. 6. (a) MBL cloud fraction and effective cloud diameter. The cloud fractions for all MBL cloud scenes are binned by ln(C_D) and the medians per bin are plotted (diamonds). A sigmoid is fit to the median points (solid curve) and the coefficients provided. The fit is only applicable within the bounds of the data used for fitting, $5 \leq C_D \leq 300$ km. Contours indicate the scatter of the points about the median, where the counts per grid are normalized by the maximum grid value. Contours are 0.0, 0.1, 0.2, and 0.4. (b) Cloud spacing and effective cloud diameter. The space between clouds computed from the data. The counts per grid are normalized by the maximum grid value. Contours are 0.0, 0.1, 0.2, 0.4, 0.6, and 0.8. Line with diamonds gives the median spacing diameters per ln(C_D) bin. The vertical dashed lines delineate groupings discussed in the text.

ship shown between cloud fraction and C_D is very similar to that obtained if the fits are performed individually per region (not shown) instead of being aggregated into a single fit.

We note that other studies have shown the value in using more sophisticated techniques for MBL cloud identification and classification, such as the neural net used by Wood and Hartmann (2006). They use 32 elements describing the LWP power spectrum and 40 elements characterizing the LWP probability distribution function to classify the MCC in MODIS scenes (no MCC, closed MCC, open MCC, and cellular but disorganized). Unfortunately, ranges of our C_D values will not directly correlate with their categories because they use additional information about the LWP spatial structure that is not considered in our classification. However, smaller values of C_D will contain open MCC (among other scattered cloud types), and intermediate values will contain closed MCCs. (Below, in section 4a, these categories will be referred to respectively as "scattered" and "clumped.")

4. Results

Six years of *Terra* MODIS data from our five MBL study regions are used to investigate the long-term, broad characteristics of MBL clouds and their variability as a function of geography, season, and drizzle occurrence.

a. Cloud diameter regional and seasonal variation

The mesoscale organization of MBL clouds can be characterized using the effective cloud diameter. For ease of discussion, MBL cloud scenes are divided into the following three descriptive categories: scattered, $C_D \leq 20$ km; clumped, $20 < C_D \leq 140$ km; and overcast, $C_D > 140$ km. These values are obtained from the frequency histograms of C_D, as well as from visual inspection of plots of the horizontal distributions of the cloud mask within each category. This choice is supported further by examining the cloud spacing. The cloud spacing diameter S_D is defined as the average distance between clouds (i.e., the diameter of the holes) and is computed similarly to C_D, except the area and perimeter of the clouds [A_i and P_i in Eq. (1)] are replaced by, respectively, the area and perimeter of the N individual clear regions within the scene. Figure 6b gives the relative frequency distribution of S_D versus C_D for the data from Fig. 6a. Two local maxima in S_D versus C_D space are found at C_D values of about 60 and 200 km. These maxima (separated by the vertical lines in Fig. 6b) support the numerical values observed for the descriptive cloud categories. Further, we note that the dynamic range in C_D is much greater than S_D; for example, the maxima at 0.8 span only a twofold difference in S_D (9–20 km) while the same contour spans a fourfold difference in C_D (30–120 km). Thus, while C_D and S_D tend to be (anti) correlated, C_D's larger dynamic range suggests that it is better suited to represent the average cloud structure scene-to-scene variability.

The overall relationship between C_D and the mesoscale organization is summarized in Fig. 7, which shows the cumulative frequency distribution of MBL C_D for all regions and all years combined. The percentages of MBL scenes per category (scattered, clumped, and overcast) are approximately 15%, 60%, and 25%. Stratiform MBL clouds are often sought for natural examples of clouds that approach being plane parallel, but this figure illustrates that this is a relatively uncommon state for MBL clouds and emphasizes the importance of broken (i.e., either scattered or clumped) MBL cloud scenes over the major MBL cloud regions of the globe. Such broken regions may be influenced by the occurrence of POCs and the physical processes operating therein.

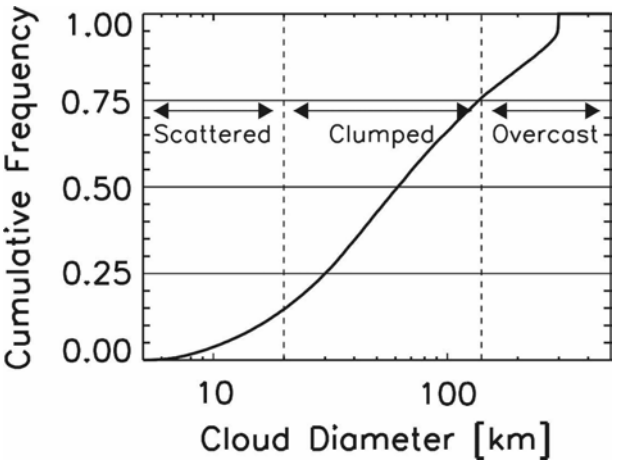

FIG. 7. Cumulative frequency of occurrence of MBL effective cloud diameters. All regions and years combined in the plot. For ease of discussion, cloud scenes are divided into three descriptive categories: scattered, $C_D \leq 20$ km; clumped, $20 < C_D \leq 140$ km; and overcast, $C_D > 140$ km. The percentages of MBL scenes per category (scattered, clumped, and overcast) are approximately 15%, 60%, and 25%.

The five MBL cloud regions explored in this study show two distinct modes of C_D frequency of occurrence. Figure 8a shows the partitioning of the scattered, clumped, and overcast MBL cloud categories for each of the five regions combining all years. MBL cloud scenes observed for the Peru, California, and Angola regions are similar in nature, that is, for all three regions the greatest fraction of clouds are clumped (~65%), and there are more overcast scenes (~25%) compared to scattered scenes (~10%). For Australia and the Canary Islands, there are greater fractions of scattered scenes at the expense of overcast scenes. This is consistent with the observations by Norris (1998) that showed a greater occurrence of broken clouds in these regions, and with Klein and Hartmann (1993) who show that the Canary Islands and Australia regions have relatively lower amounts of stratus, stratocumulus, and sky-obscuring fog compared to the other regions.

To investigate the differences in cloud structure with seasonal cycle and its variation among the regions, we determine the fraction of the scenes per month within the three different ranges of C_D, and show the fractions per category as a function of the seasonal cycle (Figs. 8b–f). The California, Peru, and Angola regions are dominated by clumped clouds, and the fractions of overcast clouds increase during the peak months at the expense (reduction) of clumped and scattered cloud fraction. The Canary Islands and Australia regions exhibit larger amplitudes in their seasonal cycle of scattered cloud with the maximum (minimum) frequencies

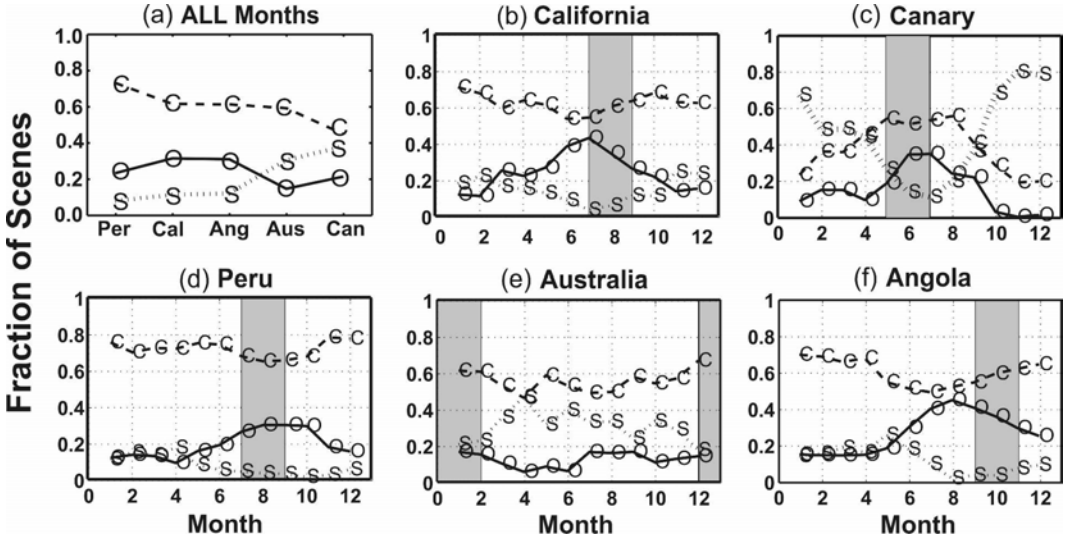

FIG. 8. General MBL cloud structure per region. (a) All years and months are combined per region to show the total composition of each study region given as a fraction of the three descriptive cloud categories: scattered (S), clumped (C), and overcast (O). (b)–(f) Seasonal cycle of MBL cloud structure per study region. The relative frequency of occurrence per month is given for each of the three cloud categories. Gray shading indicates the 3 months of peak MBL cloud occurrence per region.

of scattered (clumped) clouds occurring during the off-peak (peak) months. This has important implications for the parameterization of these cloud types in climate models because these different cloud categories have very different impacts on the energy and water balance of the ocean–atmosphere system and likely are influenced by different dynamical mechanisms.

A more quantitative assessment of the differences in C_D between regions and seasons is shown in Fig. 9, which gives the relative frequency of occurrence of C_D for all regions (Figs. 9a,b). The frequencies are partitioned by the three peak months of MBL cloud occurrence (defined in Table 1) and the nine off-peak months. These plots show two distinct groups of regional characteristics, where California, Peru, and Angola form one group, and Australia and the Canary Islands form the other. The distributions of the California group tend to have larger C_D than the Australia group (during both peak and off-peak months), and the Australia group has a much larger fraction of C_D less than 20 km. This is consistent with the greater fraction of scattered clouds in the Australia and Canary Islands regions shown in Fig. 8a. Figures 9c,d clarify the differences in the frequency distributions of C_D between peak and off-peak months using the California and Australia regions. In both regions there is a clear shift toward larger values of C_D during the peak months (i.e., there is a greater proportion of overcast cloud scenes). Similar plots for Angola, Australia, and Peru (not shown) reveal similar shifts.

b. Relation to scene drizzle occurrence

Previous studies of MBL cloud systems show that the presence of satellite-observed cloud particle effective radii greater than 15 μm generally indicates the presence of drizzle (Pinsky and Khain 2002; Masunaga et al. 2002; Shao and Liu 2004). Such a threshold cannot treat some of the finer details of drizzle occurrence (such as drizzle rate) and, in certain cases, it might even be unable to detect drizzle that occurs at the base of a thick cloud that has not yet involved (entrained) the higher cloud levels in the precipitation process. Nevertheless, because we lack a comprehensive picture of drizzle occurrence within broader MBL cloud systems, even a crude threshold can provide valuable insights into how common drizzle is within MBL cloud systems, the degree of its seasonal and regional variations, as well as the coincident variation in the other cloud microphysical properties. Thus, we adopt this threshold and, in its application, require that the scene-mean R_{eff} is greater than or equal to 15 μm for the *scene* to be identified as drizzling. This is a rather stringent requirement because drizzle-sized droplets must occur over a majority of a GCM-sized grid box and, thus, is only used to identify scenes that have a pronounced drizzle mode.

We tested the sensitivity of our drizzle frequencies to the R_{eff} at cloud edges that, as discussed before, may carry greater uncertainty from edge and 3D effects. We compared the frequency distributions of scene drizzle occurrence when more than one ring was removed (not

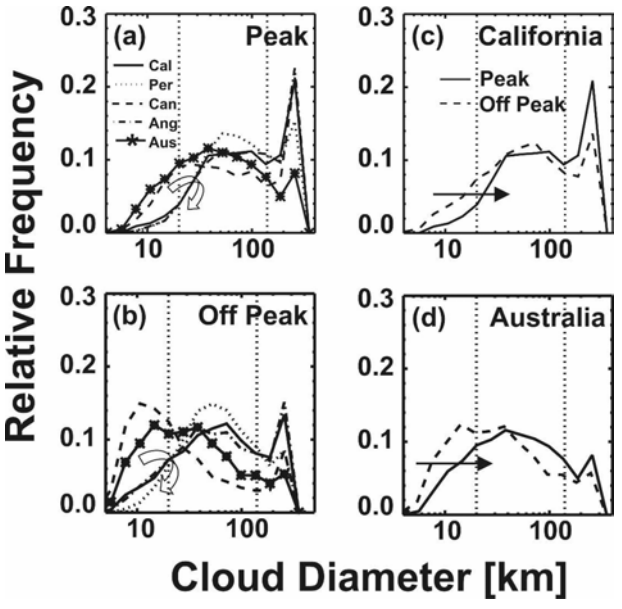

FIG. 9. Relative frequencies of occurrence of C_D per region. (left) All regions are placed on one plot partitioned by (top) peak and (bottom) nonpeak months of MBL cloud occurrence. Semicircles encompass California, Peru, and Angola, which have similar distributions that are distinctively different from the features shared by the Canary Islands and Australia. (right) Results for the (top) California and (bottom) Australia regions, partitioned by the three peak (solid) and nine nonpeak (dashed) months. A shift toward larger cloud diameters occurs during the peak months (including the regions not shown).

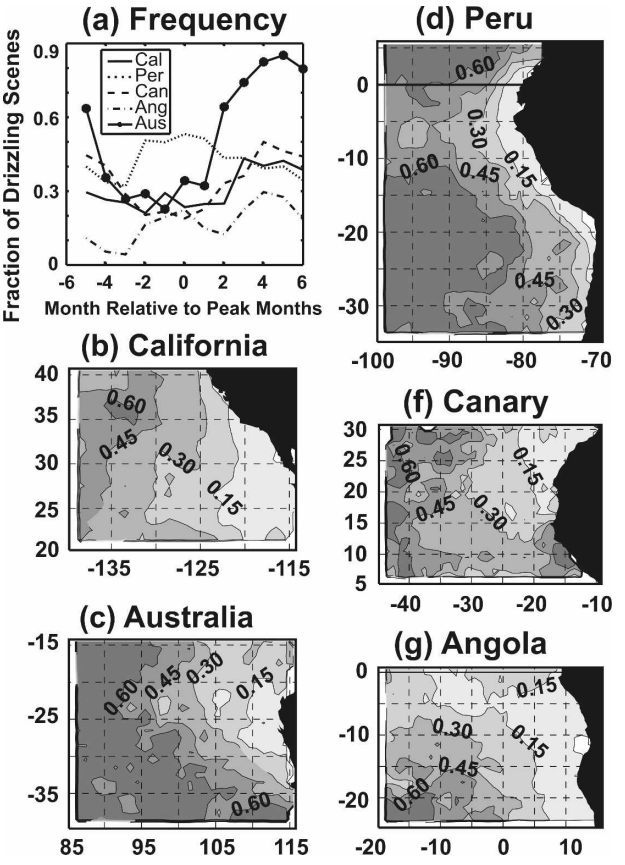

FIG. 10. Geographical distribution of drizzle frequency. Drizzle scenes are defined as those with a mean $R_{\text{eff}} \geq 15$ μm (Pinsky and Khain 2002; Masunaga et al. 2002; Shao and Liu 2004). (a) Monthly variation of drizzle frequency. Plotted are the fractions of MBL scenes that meet the drizzle criterion per month. The abscissa is the month of year, given per region as an offset relative to the middle of its three peak months (given in Fig. 8 and Table 1). (b)–(f) Regional distribution of drizzling MBL cloud scenes. Shown are the fractions of MBL scenes that are drizzling per grid, where the scenes for all months are combined in a single grid per region. Contours of fractional occurrence are given for 0.15, 0.30, 0.45, and 0.60. Note that the total drizzle occurrence would be determined by weighting these fractions by the total frequency of MBL occurrence per grid. Occurrence frequency per region is binned on a 1° grid.

shown) and found small differences at the smallest values of C_D, which were sufficiently minor that they could just be an artifact caused by elimination of some small clouds in the removal of more rings. Thus, these results suggest that the edge effects should not adversely affect our scene drizzle determination. We also considered the more detailed drizzle occurrence parameterization of Bennartz (2007). Bennartz builds upon the work of Pawlowska and Brenguier (2003), van Zanten et al. (2005), and Wood (2005) who present relationships between cloud thickness and cloud particle number concentration, which then can be related to the liquid water path, cloud fraction, optical depth, and drizzle rate. In a comparison between the number of drizzling scenes identified by the Bennartz parameterization and the 15-μm threshold, we found that only 11% of the scenes are identified differently. We remained with the 15-μm threshold because of its simplicity, and the lack of additional data for the scenes (values of adiabaticity and the condensation rate) upon which the Bennartz criterion depends critically.

Using this criterion, we determine the fraction of MBL scenes that are drizzling for the different seasons and regions. Figure 10a shows the fraction of MBL cloud scenes that have a dominant drizzle mode over 6 yr of *Terra* MODIS observations, which are shown as a function of month relative to the region's peak month. This indicates that the fraction of MBL scenes that are drizzling are generally greater during the off-peak months than for the peak months. For the California, Canary Islands, and Australia regions, the month of peak drizzle occurrence coincides with the peak fraction of scattered cloud scenes (cf. with Fig. 8). The Angola region shows a frequency of drizzle that is consistently lower than any other region, and its month for

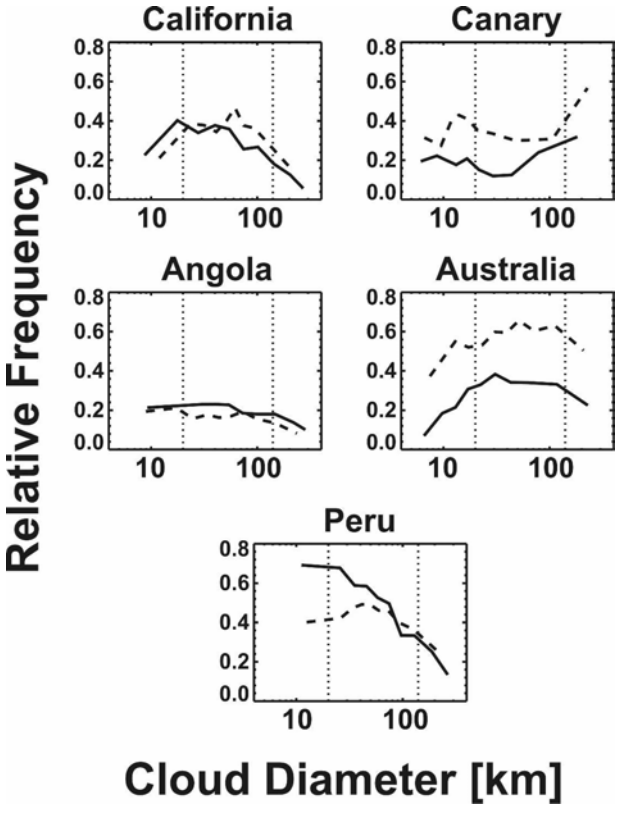

FIG. 11. Frequency of drizzle occurrence as a function of effective cloud diameter. The drizzle frequencies are partitioned into two groups: the 3 months of peak MBL cloud occurrence within each region (solid line), and the nine off-peak months (dashed line). The frequencies for California and Angola show little sensitivity to peak vs off-peak timings, while Peru and Australia show pronounced differences in directions that are opposite from each other.

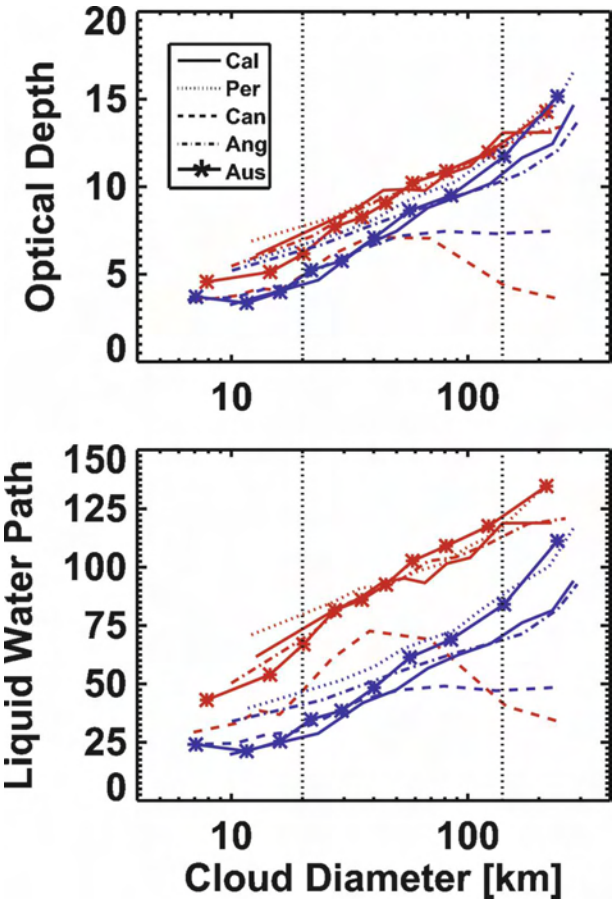

FIG. 12. Dependence of MBL cloud properties on effective cloud diameter. MBL cloud optical depth (top) τ_{vis} and (bottom) LWP are plotted as a function of the natural logarithm of C_D. For each curve, all data per region are separated into drizzling (red) and nondrizzling (blue) categories. Ten bins are used, where one-tenth of the values per curve are averaged for each point plotted.

peak drizzle does not coincide with the peak occurrence of scattered clouds (in fact, they are separated by 3 months). The former observation is consistent with the results of Masunaga et al. (2002), who suggest that this may be due to cloud–aerosol interactions. Figures 10b–f show the regional distribution of drizzling MBL cloud scenes for each region. Overall, the patterns show a tendency for the fraction of drizzling scenes to increase going away from the coast. This pattern and some of the finer details in the regional drizzle occurrence are qualitatively consistent with the results Masunaga et al. (2002) and Kawamoto et al. (2001).

To illustrate the relationship between drizzle occurrence and cloud structure further, Fig. 11 shows the frequency of drizzle occurrence as a function of C_D for each region, separated for their peak and off-peak months. The California and Peru regions have local maxima near 20 km, which suggests that an average cell size of 20 km is preferred for drizzle in these regions. The California and Angola regions have similar drizzle frequencies (as a function of C_D) for their peak and off-peak months, while Peru demonstrates dramatically larger frequencies during its peak months. The Peru pattern is opposite that for Australia and the Canary Islands, which have substantially lower drizzle frequencies during their peak months. These results indicate that there are unique patterns of drizzle occurrences among the regions, which are distinguishable by C_D and the peak versus off-peak months.

c. MBL cloud optical and microphysical properties

Figure 12 shows the variation of τ_{vis} and LWP as a function of C_D for all regions divided by drizzling and nondrizzling scenes. These plots show that, despite some interregional variations, robust trends exist between the C_D and cloud optical and microphysical

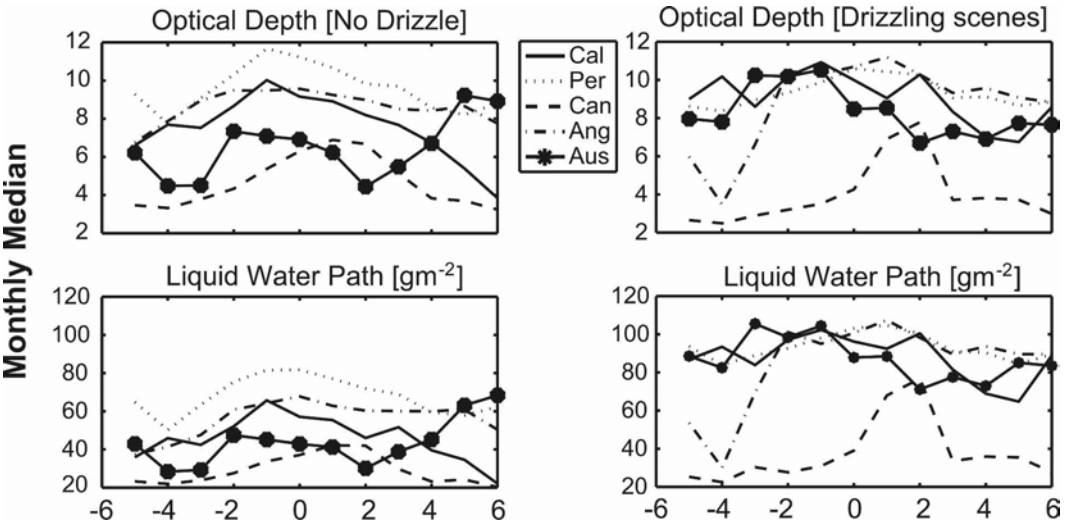

FIG. 13. Monthly variation in MBL cloud properties. For each curve, all data per region are separated into drizzling and nondrizzling categories and their monthly means are plotted. Shown are the monthly medians of MBL cloud optical depth (top) τ_{vis} and (bottom) LWP for (left) nondrizzling and (right) drizzling scenes. The abscissa is the month of year, given per region as an offset relative to the middle of its three peak months (explained in Fig. 10). The pattern shown for Peru is indicative of that found for the northern part of the study region (see text).

properties. The τ_{vis} and LWP trend strongly with C_D for all regions, with the greatest values occurring for the drizzling scenes, particularly for LWP. However, there are considerable interregional differences in the trends, indicating that different functionalities exist between the regions.

Of particular interest is the dramatically different pattern found for the Canary Islands region, which we investigated further. We verified the robustness of the result to the sensitivity to the cloud mask certainty, increasing the mask threshold for valid pixels (section 2) to the 95th percentile and arriving at the same results (for all regions). More so than the other regions, the Canary Islands region is frequently visited by dust, biomass burning aerosols, and mixtures thereof (Li et al. 2004). Previous research within this region found a positive correlation between cloud fraction and aerosol index, which would be consistent with mineral aerosols suppressing precipitation in thin low-altitude clouds (Mahowald and Kiehl 2003). However, definitive conclusions could not be drawn because the cloud and dust changes are both driven by the same meteorological conditions, and are also consistent with the misidentification of desert dust events as low-altitude thin clouds (Mahowald and Kiehl 2003). Further, we examined the seasonal variation of this bias (relative to the other regions) and found the same type of bias even during months when the climatological aerosol loading is low (e.g., see Fig. 3 in Li et al. 2004). Finally, radiative transfer studies suggest that partially absorbing aerosol layers aloft could bias the MODIS retrieval's optical depth and LWP low (Haywood et al. 2004). A biomass burning aerosol optical depth of 0.5 above the cloud reduces τ_{vis} and LWP by about 15%–20% (Bennartz and Harshvardhan 2007; Haywood et al. 2004), but this amount would only account for part of the bias found here between the Canary Islands and other regions. The effects of mineral dust on clouds are an area of active research, and clearly this is a potentially interesting case region worthy of further study.

Figure 13 shows the monthly variation in the MBL cloud optical and microphysical properties partitioned by drizzling and nondrizzling scenes. Except for Australia, the nondrizzling scenes tend to have the largest τ_{vis} and largest LWP during the region's monthly peaks. This is in phase with the increased fractional occurrence in overcast and clumped scenes (Fig. 8). The Australia region, instead, has something of a double maximum (with the largest τ_{vis} and largest LWP occurring 2 months prior to the peak, and 4 months after the peak). For drizzling scenes, the maximum values of τ_{vis} and LWP for California and Angola occur during the monthly MBL peaks, while Peru and the Canary Islands tend to occur 1 month after the peak season. The Australian region maximum tends to occur 2–4 months before its peak season.

We note that the Peru region has a much larger latitudinal range than the other regions—almost double—which may make it susceptible to north–south differences in the features discussed here. Such differences

were negligible in all prior plots; however, the seasonal patterns shown in Fig. 13 are largely driven by signals in the northern portion of the region, where the greatest fractions of the scenes were obtained (see Fig. 3). The southern portion has a signal that is phase shifted by about 6 months from that shown in Fig. 13 (top left), and lags that shown by 2 months in Fig. 13 (top right).

5. Summary and conclusions

To aid in understanding the role that MBL clouds play in climate and assist in improving their representations in climate models, we analyzed 6 yr of pixel-level *Terra* MODIS observations for five diverse regions of the globe where these cloud types are common. A feature of this study is that the long-term central tendency and seasonal variations of MBL cloud microphysical properties (e.g., LWP, R_{eff}, and optical depth) are investigated using mesoscale structure and drizzle occurrence as organizing principles. We minimize the uncertainty in the cloud microphysical retrievals that can be caused by partially filled cloud pixels or 3D effects by removing the contribution of pixels from the cloud edge (one pixel deep) from our microphysical property averages. MBL mesoscale structure is quantified using effective cloud diameter, which is introduced here as a measure of bulk cloud organization that is easy to compute and provides descriptive information beyond that offered by cloud fraction.

Despite expected differences among the regions, some similar features are found in their macroscale structure (C_D), drizzle frequency, and associated microphysical properties. The following similarities and differences may be used to target work that diagnoses MBL cloud behavior and their functional dependencies in model simulations:

1) In all regions, we find a clear seasonal cycle in the frequency of MBL cloud occurrence that is consistent with previous studies (e.g., Klein and Hartmann 1993). They concluded that this seasonal cycle was related to the boundary layer stability.
2) Although stratiform MBL clouds are often sought for natural examples of clouds that approach being plane parallel, we find overall that this is a relatively uncommon MBL state (~25%), which emphasizes the importance of accurately representing the subgrid-scale broken (i.e., either scattered or clumped) MBL cloud scenes in climate models.
3) The C_D is related to the seasonal cycle, with the greatest mesoscale organization (largest values of C_D) tending to occur during the months of peak cloud occurrence. Among the regions, the C_D frequency distributions of peak and off-peak months cluster into two groups that possess similar characteristics, with Australia and the Canary Islands in one group (which favors smaller C_D), and Angola, California, and Peru in the other.
4) The seasonal cycle of drizzle occurrence is usually at a minimum during the months of peak MBL cloud occurrence and at a maximum during the off-peak months. This would be consistent with the correlation of the largest drizzle frequencies occurring for the smaller values of C_D. Interestingly, however, the Peru region runs contrary to this pattern shared by the other four regions.
5) The patterns of drizzle frequency as a function of C_D show marked differences between the regions for peak versus off-peak months. California and Angola have drizzle frequencies that are rather independent of these two seasons, which suggests that a single PDF of drizzle frequency (versus C_D) might be used in climate models [e.g., by estimating C_D from cloud fraction using Eq. (1)].
6) However, the pattern can be quite different for the other three regions. The drizzle frequencies are greatest for the Peru region and during its peak months of MBL occurrence, which is the reverse of the off-peak timing of peak drizzle frequency for the Canary Islands and Australia. These regional contrasts may serve as an excellent test for model simulations of MBL drizzle occurrence.
7) The frequency of drizzle occurrence for the California and Peru regions tend to have pronounced maxima near a C_D of 20 km, which suggests that, in these regions, an average cell size of 20 km is preferred for drizzle. This implies that cloud resolving models may lack the horizontal resolution needed to simulate these processes and, therefore, require large-eddy simulation models until adequate parameterizations have been determined.
8) Cloud LWP and visible optical depth trend strongly with C_D, with the greatest values occurring for the drizzling scenes. However, there are considerable interregional differences in the trends, indicating that different regressions must be used for each region. Of particular note is the Canary Islands region, which, unlike the other regions, ceases to increase monotonically for $C_D > 50$ km. The explanation for this difference is the subject of future research activities.
9) The long-term cloud microphysical properties are also related to this seasonal cycle, where a region's monthly peak MBL frequency tends to have the largest mean τ_{vis} and LWP. Only the Australian region contradicts this pattern, with the larger op-

tical properties found mostly in the off-peak months.

10) Overall, the Canary Islands and Australia regions generally have similar features that are distinctively different from the other regions. They have a greater variation in their seasonal cycle of cloud structure and a larger frequency of scattered cloud scenes, which have lower τ_{vis} and low LWP. These features are in stark contrast to those from Angola and Peru, which have a greater fraction of clumped and overcast clouds that have a larger mean τ_{vis} and LWP. The California region tends to follow the seasonal pattern shared by Angola and Peru, but with lower values of mean τ_{vis} and LWP.

We note that the *Terra* orbit and types of MODIS data used here enable observing the MBL cloud state at approximately the same midmorning local time each day (about 1030 LT). However, given the long-term statistics compiled for multiple locations and seasons, we likely capture MBL states that can occur at any point during the diurnal cycle. Also, the variability of MBL cloud properties are dominated by seasonal to annual time scales, and daily to monthly time scales have smaller (but not negligible) variability (Rozendaal and Rossow 2003). Thus, our temporal sampling can capture the dominant variations in MBL cloud properties, although our sampling will favor any subtleties that occur during the midmorning hours. We also note that our definition of drizzling MBL cloud scenes is subject to several assumptions about the vertical structure of droplet sizes within a cloud layer and how it is related to the drizzle process. Although aerosol–cloud interactions are known to play an important role in MBL cloud microphysics, we have not yet included aerosol observations in our analysis.

The variability of these MBL cloud micro- and macroscale properties will have important impacts on the transfer of radiation through the atmosphere and its subsequent impact on the earth's energy balance. Future work will explore the relationships between these MBL cloud properties, the aerosol properties, the large-scale meteorological state, and the accurate representation of the associated radiative transfer in global climate models.

Acknowledgments. This work is supported by GWEC Grant NASA NAG511716 and the Department of Energy Atmospheric Radiation Measurement Program. The data used in this study were acquired as part of the NASA's Earth Science Enterprise. Dr. Collins' contributions were supported by the Director, Office of Science, at the U.S. Department of Energy under Contract DE-AC02-05CH11231. The retrieval algorithms were developed by the MODIS Science Teams. The raw data were processed by the MODIS Adaptive Processing System (MODAPS) and Goddard Distributed Active Archive Center (DAAC), and are archived and distributed by the Goddard DAAC. We would also like to thank two anonymous reviewers whose comments and suggestions have been very helpful.

REFERENCES

Agee, E. M., 1984: Observations from space and thermal convection: A historical perspective. *Bull. Amer. Meteor. Soc.,* **65,** 938–949.

Bender, F. A.-M., H. Rodhe, R. J. Charlson, A. M. L. Ekman, and N. Loeb, 2006: 22 views of the global albedo—Comparison between 20 GCMs and two satellites. *Tellus,* **58A,** 320–330, doi:10.1111/j.1600-0870.2006.00181.x.

Bennartz, R., 2007: Global assessment of marine boundary layer cloud droplet number concentration from satellite. *J. Geophys. Res.,* **112,** D02201, doi:10.1029/2006JD007547.

——, and Harshvardhan, 2007: Correction to "Global assessment of marine boundary layer cloud droplet number concentration from satellite." *J. Geophys. Res.,* **112,** D16302, doi:10.1029/2007JD008841.

Bony, S., and J.-L. Dufresne, 2005: Marine boundary layer clouds at the heart of tropical cloud feedback uncertainties in climate models. *Geophys. Res. Lett.,* **32,** L20806, doi:10.1029/2005GL023851.

Bréon, F. M., and M. Doutriaux-Boucher, 2005: A comparison of cloud droplet radii measured from space. *IEEE Trans. Geosci. Remote Sens.,* **43,** 1796–1805.

Chang, F.-L., and Z. Li, 2003: Retrieving vertical profiles of water-cloud droplet effective radius: Algorithm modification and preliminary application. *J. Geophys. Res.,* **108,** 4763, doi:10.1029/2003JD003906.

Coakley, J. A., M. A. Friedman, and W. R. Tahnk, 2005: Retrieval of cloud properties for partly cloudy imager pixels. *J. Atmos. Oceanic Technol.,* **22,** 3–17.

Comstock, K. K., C. S. Bretherton, and S. E. Yuter, 2005: Mesoscale variability and drizzle in Southeast Pacific stratocumulus. *J. Atmos. Sci.,* **62,** 3792–3807.

——, S. E. Yuter, R. Wood, and C. S. Bretherton, 2007: The three-dimensional structure and kinematics of drizzling stratocumulus. *Mon. Wea. Rev.,* **135,** 3767–3784.

Cornet, C., J.-C. Buriez, J. Riedi, H. Isaka, and B. Guillemet, 2005: Case study of inhomogeneous cloud parameter retrieval from MODIS data. *Geophys. Res. Lett.,* **32,** L13807, doi:10.1029/2005GL022791.

Cusack, S., J. M. Edwards, and R. Kershaw, 1999: Estimating the subgrid variance of saturation, and its parameterization for use in a GCM cloud scheme. *Quart. J. Roy. Meteor. Soc.,* **125,** 3057–3076.

Garay, M., R. Davies, C. Averill, and J. Westphal, 2004: Actinoform clouds: Overlooked examples of cloud self-organization at the mesoscale. *Bull. Amer. Meteor. Soc.,* **85,** 1585–1594.

Hartmann, D. L., M. E. Ockert-Bell, and M. L. Michelsen, 1992: The effect of cloud type on earth's energy balance: Global analysis. *J. Climate,* **5,** 1281–1304.

Haywood, J. M., S. R. Osborne, and S. J. Abel, 2004: The effect of

overlying absorbing aerosol layers on remote sensing retrievals of cloud effective radius and cloud optical depth. *Quart. J. Roy. Meteor. Soc.,* **130,** 779–800.

Kawamoto, K., T. Nakajima, and T. Y. Nakajima, 2001: A global determination of cloud microphysics with AVHRR remote sensing. *J. Climate,* **14,** 2054–2068.

King, M. D., S.-C. Tsay, S. E. Platnick, M. Wang, and K.-N. Liou, 1998: Cloud retrieval algorithms for MODIS: Optical thickness, effective radius and thermodynamic phase. MODIS Algorithm Theoretical Basis Document ATBD-MOD-05, 83 pp.

——, and Coauthors, 2003: Cloud and aerosol and water vapor properties, perceptible water, and profiles of temperature and humidity from MODIS. *IEEE Trans. Geosci. Remote Sens.,* **41,** 442–458.

Klein, S. A., and D. L. Hartmann, 1993: The seasonal cycle of low stratiform clouds. *J. Climate,* **6,** 1587–1606.

Li, F., A. M. Vogelmann, and V. Ramanathan, 2004: Saharan dust aerosol radiative forcing measured from space. *J. Climate,* **17,** 2558–2571.

Loeb, N. G., and R. Davies, 1996: Observational evidence of plane parallel model biases: Apparent dependence of cloud optical depth on solar zenith angle. *J. Geophys. Res.,* **101,** 1621–1634.

——, and J. A. Coakley Jr., 1998: Inference of marine stratus cloud optical depths from satellite measurements: Does 1D theory apply? *J. Climate,* **11,** 215–233.

Mahowald, N. M., and L. M. Kiehl, 2003: Mineral aerosol and cloud interactions. *Geophys. Res. Lett.,* **30,** 1475, doi:10.1029/2002GL016762.

Marshak, A., S. Platnick, T. Várnai, G. Wen, and R. F. Cahalan, 2006: Impact of three-dimensional radiative effects on satellite retrievals of cloud droplet sizes. *J. Geophys. Res.,* **111,** D09207, doi:10.1029/2005JD006686.

Masunaga, H., T. Y. Nakajima, T. Nakajima, M. Kachi, and K. Suzuki, 2002: Physical properties of maritime low clouds as retrieved by combined use of Tropical Rainfall Measuring Mission (TRMM) Microwave Imager and Visible/Infrared Scanner 2. Climatology of warm clouds. *J. Geophys. Res.,* **107,** 4367, doi:10.1029/2001JD001269.

Matsui, T., H. Masunaga, S. M. Kreidenweis, R. A. Pielke Sr., W.-K. Tao, M. Chin, and Y. J. Kaufman, 2006: Satellite-based assessment of marine low cloud variability associated with aerosol, atmospheric stability, and the diurnal cycle. *J. Geophys. Res.,* **111,** D17204, doi:10.1029/2005JD006097.

Mechem, D. B., and Y. L. Kogan, 2003: Simulating the transition from drizzling marine stratocumulus to boundary layer cumulus with a mesoscale model. *Mon. Wea. Rev.,* **131,** 2342–2360.

Menzel, W. P., B. A. Baum, K. I. Strabala, and R. A. Frey, 2002: Cloud top properties and cloud phase algorithm theoretical basis document. MODIS Algorithm Theoretical Basis Document ATBD-MOD-04, 61 pp.

Miles, N. L., J. Verlinde, and E. E. Clothiaux, 2000: Cloud droplet size distributions in low-level stratiform clouds. *J. Atmos. Sci.,* **57,** 295–311.

Naud, C. M., J.-M. Muller, E. E. Clothiaux, B. A. Baum, and W. P. Menzel, 2005: Intercomparison of multiple years of MODIS, MISR and radar cloud-top heights. *Ann. Geophys.,* **23,** 2415–2424.

Norris, J. R., 1998: Low cloud type over the ocean from surface observations. Part II: Geographical and seasonal variations. *J. Climate,* **11,** 383–403.

——, and C. B. Leovy, 1994: Interannual variability in stratiform cloudiness and sea surface temperature. *J. Climate,* **7,** 1915–1925.

Oreopoulos, L., and R. Davies, 1998: Plane-parallel albedo biases from satellite observations. Part II: Parameterizations for bias removal. *J. Climate,* **11,** 933–944.

Pawlowska, H., and J.-L. Brenguier, 2003: An observational study of drizzle formation in stratocumulus clouds for general circulation model (GCM) parameterizations. *J. Geophys. Res.,* **108,** 8630, doi:10.1029/2002JD002679.

Petters, M. D., J. R. Snider, B. Stevens, G. Vali, I. Faloona, and L. M. Russell, 2006: Accumulation mode aerosol, pockets of open cells, and particle nucleation in the remote subtropical Pacific marine boundary layer. *J. Geophys. Res.,* **111,** D02206, doi:10.1029/2004JD005694.

Pinsky, M. B., and A. P. Khain, 2002: Effects of in-cloud nucleation and turbulence on droplet spectrum formation in cumulus clouds. *Quart. J. Roy. Meteor. Soc.,* **128,** 501–534.

Platnick, S., M. D. King, S. A. Ackerman, W. P. Menzel, B. A. Baum, J. C. Riedi, and R. A. Frey, 2003: The MODIS cloud products: Algorithms and examples from Terra. *IEEE Trans. Geosci. Remote Sens.,* **41,** 459–473.

Randall, D. A., J. A. Coakley, C. W. Fairall, R. A. Kropfli, and D. H. Lenshow, 1984: Outlook for research on subtropical marine stratiform clouds. *Bull. Amer. Meteor. Soc.,* **65,** 1209–1301.

Rosenfeld, D., Y. J. Kaufman, and I. Koren, 2006: Switching cloud cover and dynamical regimes from open to closed Benard cells in response to the suppression of precipitation by aerosols. *Atmos. Chem. Phys.,* **6,** 2503–2511.

Rozendaal, M. A., and W. B. Rossow, 2003: Characterizing some of the influences of the general circulation on subtropical marine boundary layer clouds. *J. Atmos. Sci.,* **60,** 711–728.

Shao, H., and G. Liu, 2004: Detecting drizzle in marine warm clouds using combined visible, infrared, and microwave satellite data. *J. Geophys. Res.,* **109,** D07205, doi:10.1029/2003JD004286.

Sharon, T. M., B. A. Albrecht, H. H. Jonsson, P. Minnis, M. M. Khaiyer, T. M. van Reken, J. Seinfeld, and R. Flagan, 2006: Aerosol and cloud microphysical characteristics of rifts and gradients in maritime stratocumulus clouds. *J. Atmos. Sci.,* **63,** 983–997.

Stevens, B., G. Vali, K. Comstock, R. Wood, M. C. van Zanten, P. H. Austin, C. S. Bretherton, and D. H. Lenschow, 2005: Pockets of open cells (POCs) and drizzle in marine stratocumulus. *Bull. Amer. Meteor. Soc.,* **86,** 51–57.

Vant-Hull, B., A. Marshak, L. A. Remer, and Z. Q. Li, 2007: The effects of scattering angle and cumulus cloud geometry on satellite retrievals of cloud droplet effective radius. *IEEE Geosci. Remote Sens.,* **45,** 1039–1045.

van Zanten, M. C., B. Stevens, G. Vali, and D. Lenschow, 2005: Observations of drizzle in nocturnal marine stratocumulus. *J. Atmos. Sci.,* **62,** 88–106.

Várnai, T., and A. Marshak, 2002a: Observations and analysis of three-dimensional radiative effects that influence MODIS cloud optical thickness retrievals. *J. Atmos. Sci.,* **59,** 1607–1618.

——, and ——, 2002b: Observations of three-dimensional radiative effects that influence satellite retrievals of cloud properties. *Idojaras,* **106,** 265–278.

Wood, R., 2005: Drizzle in stratiform boundary layer clouds. Part

I: Vertical and horizontal structure. *J. Atmos. Sci.,* **62,** 3011–3033.

——, and D. L. Hartmann, 2006: Spatial variability of liquid water path in marine low cloud: The importance of mesoscale cellular convection. *J. Climate,* **19,** 1748–1764.

Woodruff, S. D., R. J. Slutz, R. L. Jenne, and P. M. Steurer, 1987: A comprehensive ocean–atmosphere data set. *Bull. Amer. Meteor. Soc.,* **68,** 1239–1250.

Xu, K.-M., T. Wong, B. A. Wielicki, L. Parker, and Z. A. Eitzen, 2005: Statistical analyses of satellite cloud object data for large ensemble evaluation of cloud models. Part I: Methodology and preliminary results. *J. Climate,* **18,** 2497–2514.

Zhang, M. H., and Coauthors, 2005: Comparing clouds and their seasonal variations in 10 atmospheric general circulation models with satellite measurements. *J. Geophys. Res.,* **110,** D15S02, doi:10.1029/2004JD005021.

Zhou, M., X. Zeng, M. Brunke, Z. Zhang, and C. Fairall, 2006: An analysis of statistical characteristics of stratus and stratocumulus over eastern Pacific. *Geophys. Res. Lett.,* **33,** L02807, doi:10.1029/2005GL024796.